Wave propagation in mechanical metamaterials

Zhou, Y.; Zhou Y.

Chapter 2

Kink-antikink asymmetry in topological mechanical chains

2.1 Introduction

Topological ideas have led to recent advances in continuum mechanics often inspired by the physics of electronic topological insulators and the quantum Hall effect. In these electronic systems the basic question is whether a material is an insulator or a conductor. The answer depends on which portion of a topological insulator one examines: the bulk is usually gapped and hence insulating while the edge displays gapless edge modes whose existence is protected from disorder and variations in material parameters by the existence of integer-valued topological invariants [54]. In topological mechanical systems, the corresponding question is whether a material is rigid or floppy. The ability to modulate the rigidity of a structure in space allows to robustly localize the propagation of sound waves [17, 29–42, 47, 55, 56], change shape in selected portions [13, 18, 19, 25, 26, 28, 43–46] or focus stress leading to selective buckling or failure [14].

By translating the topological properties of bands of electronic states into the classical setting of vibrational bands, one can identify topologically

protected and hence robust properties of vibrational modes in both discrete lattices and continuous media. For example, the concept of "topological polarization" recently introduced by Kane and Lubensky [25] building on counting ideas from Maxwell and Calladine [57, 58] determines the existence and the position of zero-energy motions that are localized at edges and defects of a marginally rigid mechanical lattice (one in which constraints and degrees of freedom are exactly balanced).

Perhaps the simplest model of topological mechanical lattices is the rotor chain proposed in Ref. [25]. The system consists of a chain of classical rotors harmonically coupled with their nearest neighbours, as shown in Fig. 2.1a. There are two distinct classes of ground state configurations, one with all rotors leaning towards the left and the other where they lean towards the right. Mathematically, these two states may not be deformed to each other without the appearance of bulk zero modes; thus they may each be assigned a different winding number, associated with the Fourier transform of the compatibility matrix $C(q)$, which connects the linear displacement of rotors with the extension of springs; see Ref. [26] for a detailed explanation.

The above considerations arise from band theory and thus concern only the linearized zero-energy infinitesimal motions. Indeed, the vanishing of the linear response implies that nonlinear effects dominate. By developing a nonlinear theory of the rotor chain, it was shown in Ref. [18] that the infinitesimal zero-mode displacement integrates to a finite motion. This motion can be described in the continuum limit by objects similar to "kinks" in the ϕ^4 field theory [50], which connects the topological polarization invariant of the linear vibrations to the study of topological solitons [18, 19]. Although the two appearances of the term "topology" in the linear and nonlinear theory stem from different contexts, the latter encompasses the predictions of the former and also explains additional features exclusive to the nonlinear dynamics [19].

The nonlinear dynamics of this topological chain can be approximated by the critical trajectories of a Lagrangian written in the following form [18, 19]

$$L = \int \mathrm{d}x \quad \underbrace{\left(\frac{\partial u}{\partial t}\right)^2}_{\text{the kinetic term}} - \underbrace{\left(\frac{\partial u}{\partial x}\right)^2 - \frac{1}{2}(u^2-1)^2}_{\text{the classical } \phi^4 \text{ potential terms}} - \underbrace{\sqrt{2}\,\frac{\partial u}{\partial x}(u^2-1)}_{\text{the topological boundary term}} \quad . \tag{2.1}$$

The first term corresponds to the kinetic energy while the second and third are the ones encountered for example in the Landau theory of the Ising model. Note, however, that there is an additional boundary term that contributes to the energy but does not enter the Euler-Lagrange equation. Hence, one obtains static kink and antikink solitary wave solutions of the usual form [50]

$$u = \pm \tanh\left(\frac{x - x_0}{\sqrt{2}}\right). \tag{2.2}$$

The boundary term gives new properties to the solutions and breaks the symmetry between kinks and antikinks. For example, it predicts that the static kink configuration costs zero potential energy while the static antikink configuration has a finite potential energy. Previous work on this model has been motivated by the kink's zero-energy properties, and thus the shape and stability of the antikink and its dynamical behavior were not studied.

In this Chapter we explore the physics of these finite-energy configurations. We compare the dynamics of the kink and antikink sectors in the topological rotor chain and study their interaction with a lattice impurity. We find that differences arising from the topological boundary term are apparent in all of these aspects. In Sec. 2.2, we explain the discrete model and develop a fixed-point analysis of the kink motion using a cobweb plot. In Sec. 2.3, we review the continuum theory and compare the predictions for the antikink with the discrete model. In Sec. 2.4, we study the eigenmodes of the chain around a single kink or antikink profile. We exploit the tangent stiffness matrix approach developed by Guest [59] to analyze prestressed structures. In Sec. 2.5, we study the nonlinear transport properties. In a conventional continuum ϕ^4 field theory, owing to translation invariance, both the kink and antikink propagate at uniform speed. However, lattice discreteness effects breaks this invariance and generates the so-called Peierls-Nabarro (PN) barrier [60–62]. For the topological rotor model, we find that only the antikink has a finite PN barrier whereas the kink always propagates freely. We explain this phenomenon as a consequence of the zero-energy cost associated with the kink profile.

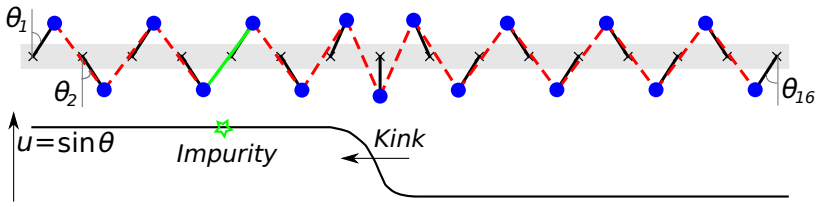

(a)

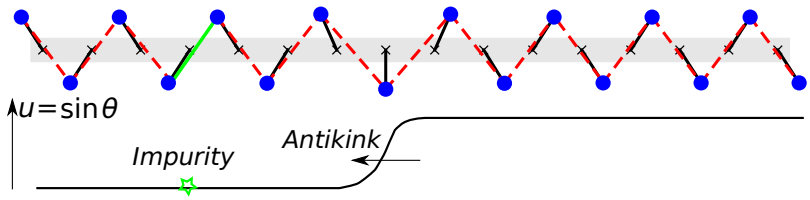

(b)

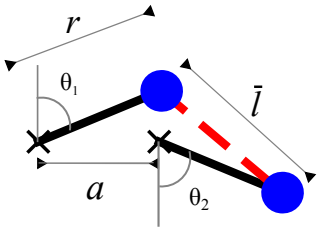

(c)

Figure 2.1. A kink (**a**) and an antikink (**b**) configuration in a topological chain (TC) model of rotors (blue) and springs (red dashed lines) in the presence of a single impurity (green solid lines) modeled as a spring with a different stiffness. For the kink profile, the springs in the chain are at their rest length, while for the antikink, they are stretched. A sketch of kink and antikink profiles in terms of the continuum field variable $u = \sin\theta$ (where θ is the rotor angle) is shown below each configuration. (**c**) A two-rotor system. The masses are the blue dots, the rigid rotors are the black lines, the pivots are the crosses, and the spring is the dashed red line. Here, a is the lattice spacing, r is the rotor length, $\bar{l}$ is the rest length of the springs and $\theta_{1,2}$ are the rotor angles with respect to the vertical.

2.2 Discrete model

The model we study consists of rotors of length r. The rotor pivots are placed on a 1D lattice with spacing a. The angles θ_i of the rotors are measured in an alternating fashion along the lattice, from the positive y-axis at odd-numbered sites and negative y-axis at even-numbered sites. The equilibrium angle is $\overline{\theta}$ for a uniform lattice configuration *without* a kink or antikink. The masses M at the tips of the rotors are connected by harmonic springs with identical rest lengths $\bar{l}$ and spring constants k. The two-rotor unit cell of the topological chain is illustrated in Fig. 2.1c.

We now construct the chain *with* a kink under free boundary conditions. There are n rotors and $n-1$ springs. If we assume that the springs are infinitely stiff ($k \to \infty$), the springs become $n-1$ constraints and the system only has a single independent degree of freedom. The angle of a single rotor determines all the others iteratively. This degree of freedom manifests itself as a mechanism which, as has been previously shown in [18], can be approximately described by the domain wall solution in a modified ϕ^4 theory [1]. We call this mechanism a "kink" and discuss its continuum theory in the following sections.

We use a cobweb plot to display the kink in Fig. 2.2. This is a tool for visualizing the process of iteratively solving the nonlinear constraint equations Eqn. (2.3) cell by cell. We construct the cobweb plot by drawing (1) a diagonal line $\theta_i = \theta_{i+1}$ and (2) a curve of the implicit function given by the nonlinear constraint equation that ensures the springs are not stretched,

$$(a + r\sin\theta_i - r\sin\theta_{i+1})^2 + (r\cos\theta_i + r\cos\theta_{i+1})^2 = \bar{l}^2. \qquad (2.3)$$

(An explicit relation between neighbouring rotor angles is derived analytically with complex notation in Appendix 2.A.)

[1] Varying the parameters $(a, r, \overline{\theta})$ yield other phases of the topological rotor chain. In this thesis, we only consider the topological chain in the *flipper* phase [18] where the ϕ^4 theory is a valid approximation. The name flipper describes the back-and-forth motion of the rotors as a kink propagates, in contrast to the *spinner* phase, where the rotors complete a full circle. The continuum limit of the spinner phase can be approximately described by the sine-Gordon theory

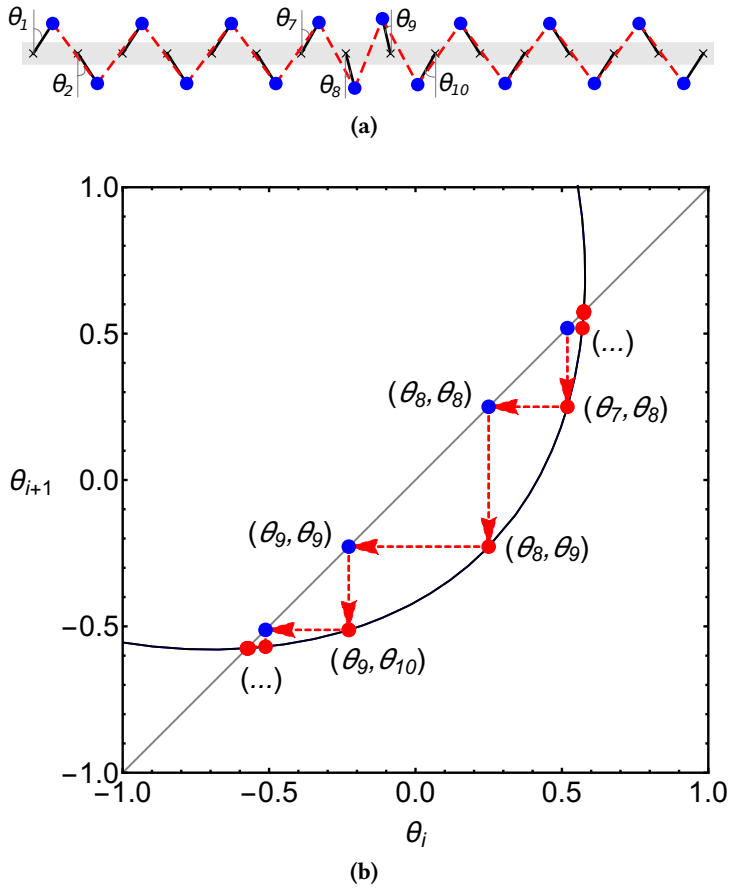

Figure 2.2. The configuration (**a**) and the corresponding cobweb plot (**b**) for the kink in a topological rotor chain with $r/a = 0.8$, $|\bar{\theta}| = 0.58$. The springs are at their rest lengths. In (**b**), the black curve is the constraint equation which ensures that the springs are unstretched, the gray diagonal line satisfies $\theta_{i+1} = \theta_i$, the blue point (θ_i, θ_i) represents rotor i, the red point (θ_i, θ_{i+1}) represents the spring connecting rotors i and $i+1$, and the red dashed lines with arrows indicates the iterative process that generates the kink profile. The iteration steps from θ_7 to θ_{10} are shown.

The iteration steps are as follows:

1. Given the angle θ_1 of the first rotor at the left end, find the point on the

function curve with coordinates (θ_1, θ_2).

2. Draw a horizontal line from (θ_1, θ_2) to the diagonal line. This gives the point (θ_2, θ_2).

3. Draw a vertical line from (θ_2, θ_2) to the function curve. This gives the point (θ_2, θ_3).

4. Repeat step 2 and 3 until the point (θ_{n-1}, θ_n) is found.

In Fig. 2.2b, we illustrate steps 2 and 3 from θ_7 to θ_{10}, which are near the kink center. The blue point with coordinates (θ_i, θ_i) stands for the ith rotor of angle θ_i. The red point with coordinates (θ_i, θ_{i+1}) represents the state of the spring that connects the rotors of θ_i and θ_{i+1}.

Note that in Fig. 2.2b, the diagonal line and the function curve intersect at two points. They are the fixed points of iteration. If all the red points (θ_i, θ_{i+1}) stay at one fixed point, the plot represents a uniform lattice. The iteration step proceeds from the leftmost rotor of the chain to the rightmost. We see that the flow proceeds outwards from one fixed point and then inwards towards the other fixed point.

The cobweb plot may be used to graphically derive the decay lengths of zero energy deformations, as they approach their uniform limits. As mentioned above, a fixed point corresponds to an intersection between the line $\theta_i = \theta_{i+1}$ and the function curve. Note that the behavior of θ_i as it approaches a fixed point resembles a "self-similar" zigzag motion between $\theta_i = \theta_{i+1}$ and the tangent line of the function curve. This motivates linearizing the function curve around the fixed point as follows:

$$\theta_{i+1} - \overline{\theta} = F'(\overline{\theta})(\theta_i - \overline{\theta}), \tag{2.4}$$

where $\overline{\theta}$, the equilibrium angle, is also just the value of the fixed-point angle and $F'(\overline{\theta})$ is the slope of the function curve at that point (which could be computed explicitly in terms of $r, a, \bar{l}$). This equation yields that $\theta_i - \overline{\theta} \propto \exp(\log F'(\overline{\theta})i)$, or that the decay length is $|1/\log F'(\overline{\theta})|$ (the sign of $\log F'$ tells us whether the fixed point is attracting or repelling). This result recovers the penetration depth of the boundary modes computed in Ref. [18] using band theory.

In the cobweb plot, the static kink appears as a sequence of points on the function curve interpolating between a repelling and attracting fixed point. The dynamics of the kink in the cobweb plot is therefore the flow of a cascade of points between a pair of fixed points (Movie S1). While the kink propagates, the points in the middle, such as (θ_7, θ_8), (θ_8, θ_9) and (θ_9, θ_{10}), corresponding to the kink center, move more than those points close to the fixed points, corresponding to the spatially localized nature of the kinetic energy.

Generating an antikink requires a few more steps, as it stretches springs, and thus does not satisfy a constraint function that we could iteratively solve. However, the continuum theory suggests that kinks and antikinks both have the same functional profiles with only their signs reversed (see Sec. 2.3). As a result, we use the same iterative procedure as that for the kink, and then simply swap the appearances of θ_i and θ_{i+1} in Eqn. (2.3) to obtain an approximation for the antikink profile. This method is equivalent to reflecting the red points in Fig. 2.2b across the diagonal line. The antikink constructed this way is not an equilibrium configuration and has unbalanced stresses in the springs. This is because generically, the profiles of the kink and antikink are not the same in a discrete topological rotor chain. We next relax the springs using *dissipative* Newtonian dynamics to remove the unbalanced stresses and obtain a stable profile, which we show in the cobweb plot in Fig. 2.3. In that figure, the spring connections (red dots) around the core of the antikink profile (rotors 8 and 9) do not fall on the curve which corresponds to unstretched springs. This implies large spring deformations which we show explicitly in Fig. 2.4b. The amount by which the springs are stretched is symmetrical around the 8th spring, which is in accordance with the fact that a stable antikink has balanced forces on each rotor. Note that we have fixed the boundary conditions to ensure that the antikink is in mechanical equilibrium, which is not generically true. As discussed later in Sec. 2.5, this has important consequences for the PN barrier.

2.3 Continuum theory

In this section, we review the continuum approximation to the kink and antikink profiles [18] and compare these with the discrete model developed in the previous section. The discrete Lagrangian for the topological rotor chain

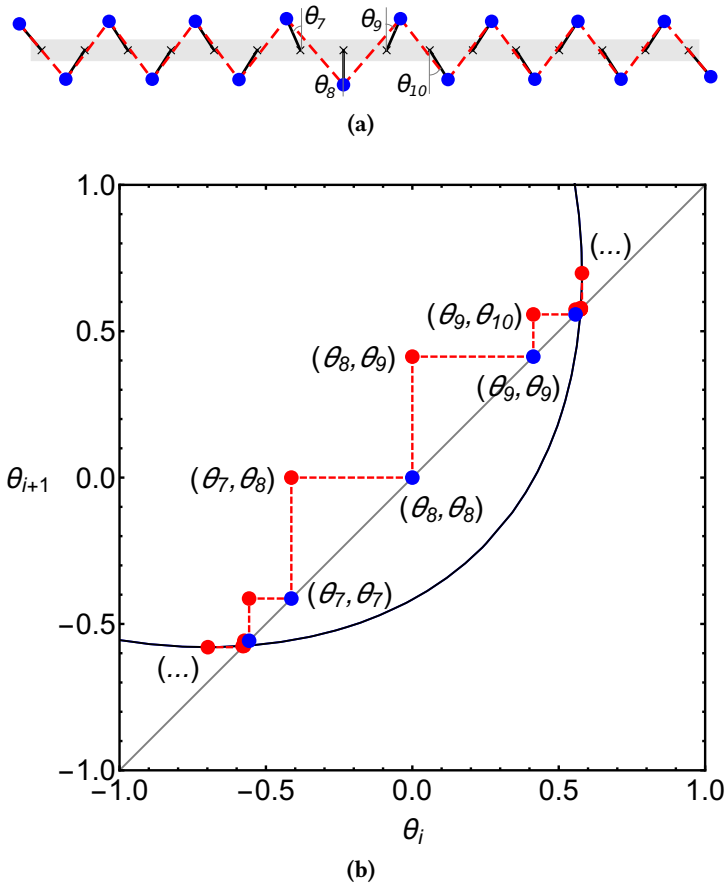

Figure 2.3. The configuration (**a**) and the corresponding cobweb plot (**b**) for an antikink profile in the topological rotor chain with $r/a = 0.8$, $|\overline{\theta}| = 0.58$, where we see that the springs are stretched. In (**b**) the same graphic notation as in Fig. 2.2 is used except that we have not used an iterative process for constructing the antikink profile, rather, depicted is only a visualization of the configuration of the rotor chain. The red points are obtained by first reflecting the red points in Fig. 2.2b across the diagonal line, and then relaxing the springs using dissipative Newtonian dynamics. Note that the two rotors at the edges need to be collinear with the springs to ensure force balance. This results in the angles overshooting at the fixed points.

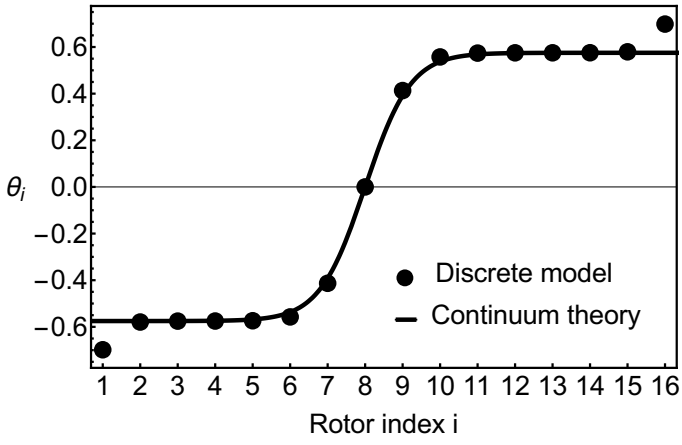

(a)

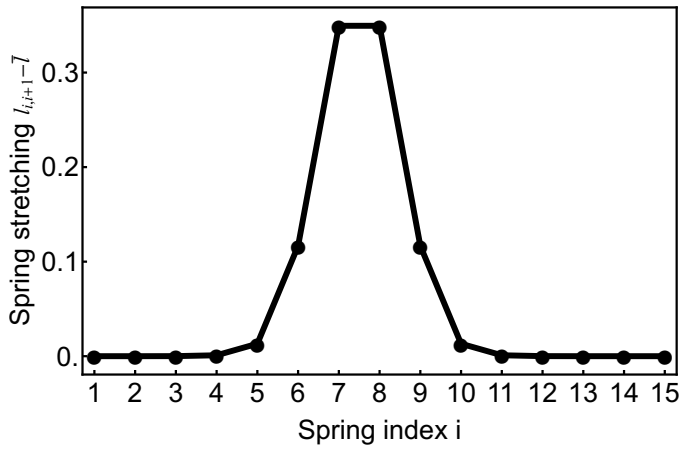

(b)

Figure 2.4. (**a**) The θ profile (rotor angles) for the antikink profile in Fig. 2.3a and the corresponding continuum prediction from Eqn. (2.13). Note that the two rotors at the edges need to be collinear with the springs to ensure force balance and this results in the rotor angles overshooting the equilibrium value $\overline{\theta} = \pm 0.58$. (**b**) The amount of spring stretching for the antikink profile.

(see also Fig. 2.2a) with free boundary conditions is

$$L = \sum_{i=1}^{n} \frac{1}{2} M r^2 \left(\frac{\mathrm{d}\theta_i}{\mathrm{d}t} \right)^2 - \sum_{i=1}^{n-1} \frac{1}{2} k (l_{i,i+1} - \bar{l})^2. \tag{2.5}$$

Here, n is the total number of rotors, M is the mass at the tip of a rotor, r is the rotor length, θ_i is the angle that rotor i makes with the vertical (measured alternately as shown in Fig. 2.2a), k is the spring constant, $\bar{l}$ is the rest length of the spring and $l_{i,i+1}$ is the instantaneous length of the spring that connects rotor i to rotor $i+1$. From geometry

$$l_{i,i+1}^2 = a^2 + 2ar(\sin\theta_{i+1} - \sin\theta_i) + 2r^2 + 2r^2\cos(\theta_i + \theta_{i+1}). \tag{2.6}$$

which in the uniform limit $\theta_i = \theta_{i+1} = \bar{\theta}$ gives the rest length of the spring $\bar{l}^2 = a^2 + 4r^2\cos^2\bar{\theta}$.

We make the working assumption that deformations do not stretch the springs significantly and hence we can neglect (or add) terms higher than quadratic order in $l_{i,i+1} - \bar{l}$ for all i. This is a reasonable approximation for the system configuration with a kink profile but is not well-justified for an antikink profile. However, in the limit that $\bar{\theta} \ll 1$, we find this to be a good approximation for both kinks and antikinks. Within this limit, we therefore express the potential energy term in Eqn. (2.5) as

$$\frac{1}{2} k (l_{i,i+1} - \bar{l})^2 \approx \frac{k}{8\bar{l}^2} \left(l_{i,i+1}^2 - \bar{l}^2 \right)^2. \tag{2.7}$$

Substituting the expression for $\bar{l}$ and Eqn. (2.6) into Eqn. (2.7), we express the potential energy as

$$V_{i,i+1} = \frac{kr^4}{2\bar{l}^2} \left(\frac{a}{r}(\sin\theta_{i+1} - \sin\theta_i) - \cos 2\bar{\theta} + \cos(\theta_i + \theta_{i+1}) \right)^2. \tag{2.8}$$

Now we take the continuum limit of the potential. First we define a continuum field for the rotor angles $\theta(x)$, where the spatial variable $x = ia + \frac{a}{2}$ is located symmetrically between two rotors in the unit cell. To leading order,

$\theta_i \to \theta(x) - (a/2)(\mathrm{d}\theta/\mathrm{d}x)$ and $\theta_{i+1} \to \theta(x) + (a/2)(\mathrm{d}\theta/\mathrm{d}x)$. Eqn. (2.8) can then be expressed as

$$aV[\theta] = \frac{2k}{\bar{l}^2}\left(\frac{a^2}{2}\frac{\mathrm{d}u}{\mathrm{d}x} + \overline{u}^2 - u^2\right)^2, \tag{2.9}$$

where we have defined the projection of the rotor position on the $x-$axis as a new field variable $u(x) \equiv r\sin\theta(x)$ and $\overline{u} \equiv r\sin\overline{\theta}$.

The kinetic energy density term in Eqn. (2.5) then assumes the form

$$aT[\dot{\theta}] = \frac{1}{2}\frac{Mr^2}{r^2 - u^2}\left(\frac{\mathrm{d}u}{\mathrm{d}t}\right)^2. \tag{2.10}$$

Next we approximate the Lagrangian Eqn. (2.5) as

$$\begin{aligned} L \approx \int \mathrm{d}x \Bigg\{ & \frac{M}{2a}\left(\frac{\partial u}{\partial t}\right)^2 - \frac{ka^3}{2\bar{l}^2}\left(\frac{\partial u}{\partial x}\right)^2 \\ & - \frac{2k}{a\bar{l}^2}(\overline{u}^2 - u^2)^2 - \frac{ka}{\bar{l}^2}\frac{\partial u}{\partial x}(\overline{u}^2 - u^2)\Bigg\}. \end{aligned} \tag{2.11}$$

where we have taken the leading order of the Taylor series expansion of the nonlinear kinetic term (in the variable u^2/r^2), which is valid in the limit when $u \ll r$ or equivalently $\sin\theta \ll 1$.

The first three terms in Eqn. (2.11) constitute the normal ϕ^4 theory. The last term linear in $\partial u/\partial x$, is an additional topological boundary term. Being a total derivative, it does not enter the Euler-Lagrange equation of motion and we obtain the usual nonlinear Klein-Gordon equation

$$\frac{M}{a}\frac{\partial^2 u}{\partial t^2} - \frac{ka^3}{\bar{l}^2}\frac{\partial^2 u}{\partial x^2} - \frac{8k}{a\bar{l}^2}\overline{u}^2 u + \frac{8k}{a\bar{l}^2}u^3 = 0, \tag{2.12}$$

whose kink and antikink solutions are given by

$$u_0 = \pm\overline{u}\tanh\left[\frac{x - x_0 - vt}{(a^2/2\overline{u})\sqrt{1 - v^2/c^2}}\right], \tag{2.13}$$

where the $\pm$ denotes an (+)antikink and (-)kink respectively. Here, v is the (anti)kink speed of propagation and $c = (a^2/\bar{l}\sqrt{k/M})$ is the speed of sound in the medium. See Fig. 2.4a for a comparison with the discrete profile.

Note how the additional boundary term makes the potential energy density $V[\theta]$ a perfect square, see Eqn. (2.9). For the kink configuration, $V[\theta]$ therefore vanishes as is the case in the discrete topological chain. For the antikink however, $V[\theta]$ is nonzero and is in fact twice of what we would expect in the normal ϕ^4 theory (where both the kink and antikink configurations have the same energy). This is an agreement with our discussion on the discrete model in Sec. 2.2.

Upon substituting the static ($v = 0$) antikink profile from Eqn. (2.13) into Eqn. (2.11) and completing the integral, we obtain the potential energy of the topological rotor chain with an antikink profile

$$V_{antikink}/(ka^2) = \frac{16}{3}\frac{(r/a)^3 \sin^3\overline{\theta}}{1 + 4(r/a)^2\cos^2\overline{\theta}}. \tag{2.14}$$

In Fig. 2.5, we compare this expression with the predictions from the discrete model. We see that the continuum theory agrees reasonably well with the discrete model as long as $\overline{\theta}$ is less than approximately 0.6, below which, the width of the antikink is larger than the lattice spacing and therefore, a continuum approximation well justified.

2.4 Linear modes

We now study small oscillations around the kink and antikink configurations, first in the continuum limit, and next in the discrete model by developing the tangent stiffness matrix approach. In the continuum limit, we make the ansatz $u = u_0 + \delta u$ and substitute into Eqn. (2.12) retaining only terms linear in δu:

$$\frac{M}{a}\frac{\partial^2 \delta u}{\partial t^2} - \frac{ka^3}{\bar{l}^2}\frac{\partial^2 \delta u}{\partial x^2} - \frac{8k}{a\bar{l}^2}(\overline{u}^2 - 3u_0^2)\delta u = 0 \tag{2.15}$$

If we Fourier transform Eqn. (2.15) with respect to time, we obtain a Schödinger-like equation with a solvable potential [63, 64]. This yields one continuous spectral band as well as two discrete modes – one translation mode for the

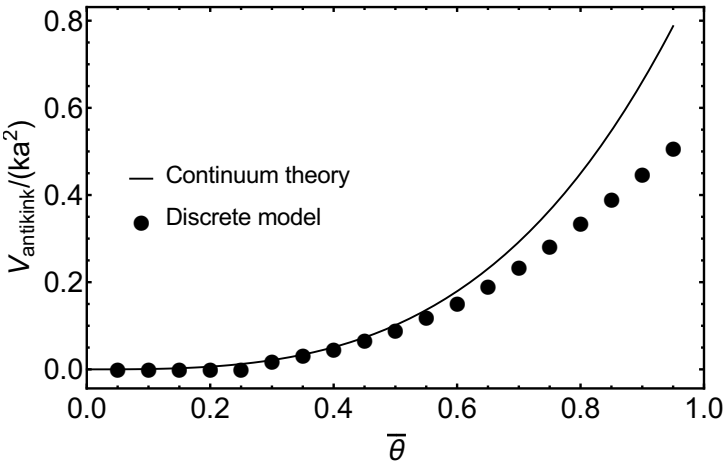

Figure 2.5. The normalized potential energy plotted against the equilibrium angle $\overline{\theta}$, for a static antikink configuration in a topological rotor chain with with $r/a = 0.8$. The discrete model has 60 rotors. Note that the wobbler transition [18] is around $\overline{\theta} = \sin^{-1}\left(\frac{a}{2r}\right) = 0.67$, which is close to where the continuum theory starts to significantly deviate from the discrete model.

(anti)kink and one shape mode [65], which corresponds to small deformations of the shape of the (anti)kink localized around the center of their profile. For the topological rotor chain, the frequencies of the two discrete modes are:

$$\omega_t = 0, \quad \text{for the translation mode} \tag{2.16}$$

$$\omega_s = (r/a)\sqrt{12k/M}\,\sin\overline{\theta}/\sqrt{1+4(r/a)^2\cos^2\overline{\theta}}, \quad \text{for the shape mode.} \tag{2.17}$$

In Fig. 2.6a and 2.6c, the kink and antikink are located in the middle of the chain. The mode arrows (in green) that all point in the same direction, correspond to a translation mode. In Fig. 2.6b and 2.6d, the arrows on either side of the (anti)kink, point in opposite directions and these correspond to shape deformations of the (anti)kink.

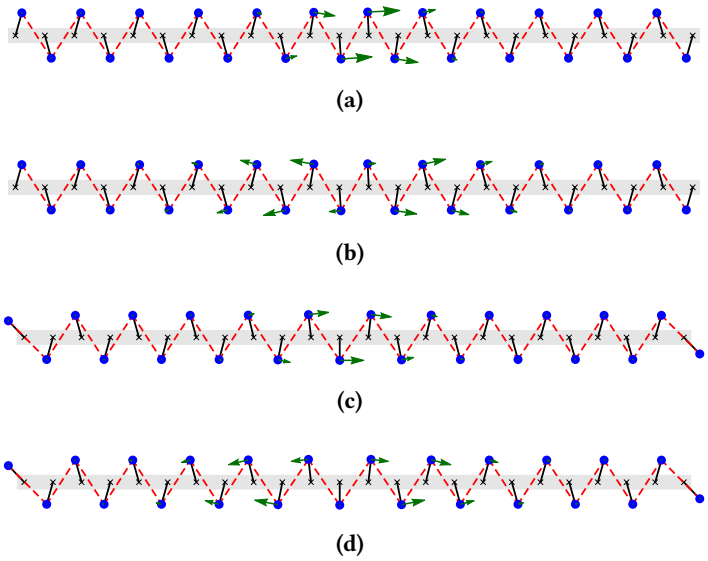

Figure 2.6. The configurations of (**a**) the kink translation mode, (**b**) the kink shape mode, (**c**) the antikink translation mode and (**d**) the antikink shape mode. The green arrows depict the mode component of each rotor.

In Appendix 2.B, we follow the approach proposed by Guest [59] to derive the *tangent stiffness matrix* $\mathbf{K}$ for prestressed mechanical structures. With $\mathbf{K}$ we numerically obtain the frequencies of localized modes for the discrete chain model and compare them with the predictions of the continuum theory (Eqn. (2.16) and Eqn. (2.17)) in Fig. 2.7. We find that the translation mode ω_t for the kink indeed vanishes (within machine-precision in our numerics) for all values of $\overline{\theta}$ and is thus absent in the range of the log-log plot shown in Fig. 2.7a). However, as seen in Fig. 2.7b, the translation mode (open circles) for the antikink is nonzero.

For the shape mode ω_s (filled circles), we find the numerical results for both the kink and antikink to be in good agreement with the continuum theory at small $\overline{\theta}$. Note that in Fig. 2.7b, although the antikink has a finite nonzero ω_t, the value is still significantly smaller than ω_s.

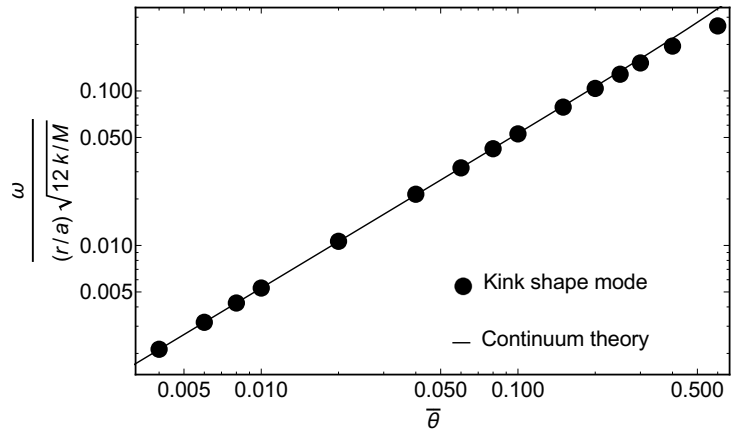

(a)

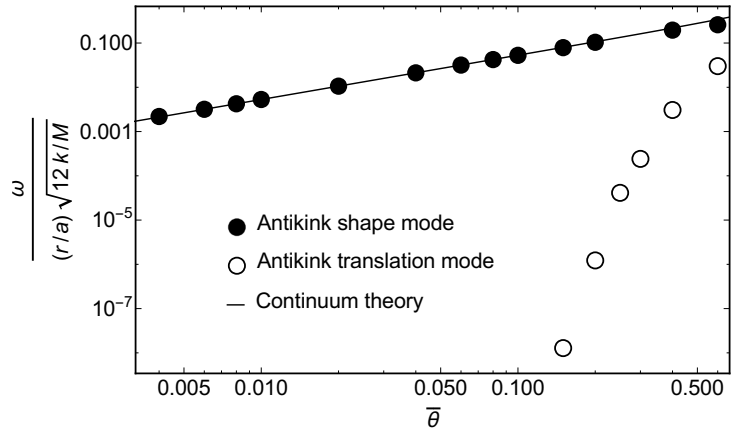

(b)

Figure 2.7. The frequencies ω of localized mode(s) for (**a**) the kink and (**b**) the antikink as a function of $\overline{\theta}$ for a rotor chain with $r/a = 0.8$. The data points are numerically obtained from the tangent stiffness matrix approach, filled circles correspond to the shape mode (ω_s), while open circles correspond to the translation mode (ω_t) . The curves are from the continuum theory. The frequencies for the kink translation mode for all $\bar{\theta}$ and the frequencies for the antikink translation mode for $\overline{\theta} < 0.1$ are effectively zero at machine precision and thus, not visible in the figure.

2.5 Nonlinear dynamics

In the previous section, we have seen that for the discrete topological chain, the energy of the translation mode for the kink is zero, whereas that for the antikink is non-zero. Note that the standard discretization of a ϕ^4 field theory leads to a non-zero translation mode for both the kink and antikink [62]. Thus, the kink here differs qualitatively from the antikink in that it has a zero mode even when we consider the discrete model. We next numerically simulate the propagation of a kink and antikink along the discrete chain and see how this difference manifests in their dynamics.

We numerically integrate Newtons equation of motion for the rotors using molecular dynamics simulations. (The simulation settings are described in Appendix 2.C.) A stable chain configuration with a single kink or antikink is used as the initial configuration (see Figs. 2.6a- 2.6c for the initial conditions used). An excitation is set in motion with a velocity along the direction of the translation mode, but with variable amplitudes.

In Fig. 2.8, we plot the kinetic energy (K.E.) of the chain as a function of time for a set of parameters, for a kink excitation (solid curve) and an antikink excitation (dashed curve). The K.E. of the kink remains nearly constant for all times with some small fluctuations (as the springs have to slightly deform to transport energy by simultaneously minimize the potential and kinetic energy). However in comparison, the K.E. of the antikink for the same set of initial parameters changes significantly as it propagates down the chain. The key point is that the kink and antikink do not propagate in the same way.

The asymmetry between a *static* kink and antikink configuration was discussed in [18]. Further, we also know from Eqn. (2.11) (and the ensuing discussion) that in the continuum limit, the topological rotor chain is approximately described by a ϕ^4 theory with an additional topological boundary term which ensures that the potential energy of the kink is zero while that for the antikink is nonzero (see Ref. [19] for an interpretation of this fact in terms of supersymmetry breaking). However, the additional boundary term does not affect the continuum equation of motion and thus, both the kink and antikink should have translational invariance in this limit and their dynamics should not have differed.

The reason for this asymmetrical behavior can be understood only if we

examine the discrete model. The system with free boundary conditions has n rotors and $n-1$ springs, and the static kink does not require any of the springs to be stretched. We can therefore interpret the springs as constraints. Thus, the discrete kink's equilibrium manifold is a continuous curve embedded in the n-dimensional configuration space of the rotor angles θ_i and the kink can be positioned stably anywhere along the chain. By contrast, an antikink requires the springs to be stretched. Forces on each of the rotors have to be balanced for the system to be in mechanical equilibrium. So the possible equilibrium configurations have to be symmetrical locally around the center of the antikink, as shown in Fig. 2.9. As a result, the equilibrium manifold for an antikink is not a continuous curve but rather, consists of a set of discrete points. These correspond to either saddle points or minima in the potential landscape. Any locally asymmetrical configuration is therefore not stable and will slide towards a minima.

The saddle points and their nearest minima can be connected by an "adiabatic trajectory" [61], which is a curve of steepest descent. The concept of an adiabatic trajectory is useful in two ways. First, it describes the slow motion of the antikink through the chain. The position of the antikink center can be defined by a coordinate along such a trajectory. Secondly, it helps to rigorously define the so-called Peierls-Nabarro (PN) potential [60–62], which is the effective periodic potential that the antikink feels as it moves along the adiabatic trajectory. A saddle point in the full potential energy landscape corresponds to a maximum along the adiabatic trajectory (while a minimum is still a minimum). Note that although the antikink's K.E. fluctuations in Fig. 2.8 do not strictly equal its PN potential barrier, the former reveals the existence of the latter.

In Appendix 2.D, we derive the PN potential barrier from the continuum theory

$$\begin{aligned} V_{PNB} &= \frac{4\pi^2\Big(\pi^2 + (a/w)^2\Big)}{3\Big(1 + 4(r/a)^2 - (a/w)^2\Big)\sinh(\pi^2 w/a)} \\ &\propto e^{-\pi^2 w/a} \qquad \text{for large } w/a. \end{aligned} \tag{2.18}$$

This shows that the PN barrier decays exponentially as the width w of the antikink increases.

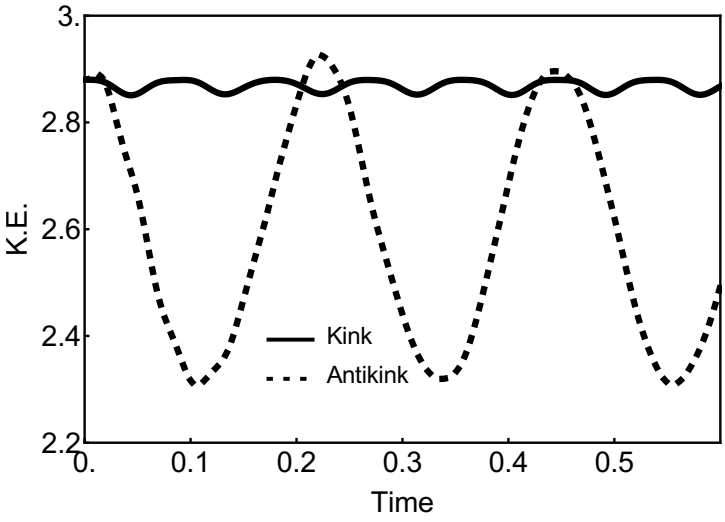

Figure 2.8. Time evolution of the kinetic energy for a kink (Fig. 2.6a) and an antikink (Fig. 2.6c) in a topological rotor chain with non-dimensional parameters $M = 1$, $k = 10000$, $r/a = 0.8$, $\overline{\theta} = 0.58$. The magnitude of initial velocity in both cases is $v_0 = 2.4$. The units of energy and velocity are determined by the aforementioned physical parameters. The kink propagation only results in small oscillation of the K.E. whereas we see significant fluctuations during the propagation of an antikink. These can be traced to the Peierls-Nabarro potential as shown in Fig. 2.9

We next compare the theoretical results with numerical simulations. We obtain the exact PN barrier by computing the difference in potential energy between the two types of equilibrium points: a minima and a saddle point, see Fig. 2.9, where for a given set of parameters, we find the barrier height to be $1359.75 - 1359.15 = 0.60$, consistent with the magnitude of the K.E. fluctuations shown in Fig. 2.8 for the same set of parameters. By repeating this calculation for systems with various antikink widths w, we obtain the dependence of the normalized PN barrier $V_{PNB}/(ka^2)$ on w/a, which we show in Fig. 2.10. We compare these with the predictions from the continuum theory, given by Eqn. (2.18). The numerical results (filled circles) obtained from the discrete lattice and the theoretical predictions (continuous curve) follow a similar trend, but differ by at least one order of magnitude. This can be explained

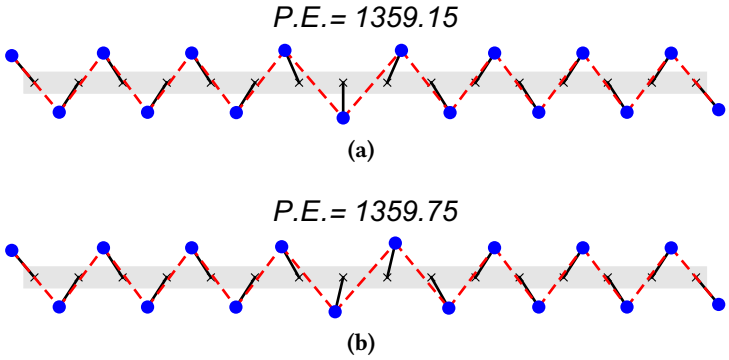

Figure 2.9. Two equilibrium configurations in the potential energy landscape of a static antikink: (**a**) a minimum and (**b**) a saddle point, respectively. The topological chain has the same configuration parameters as in Fig. 2.8.

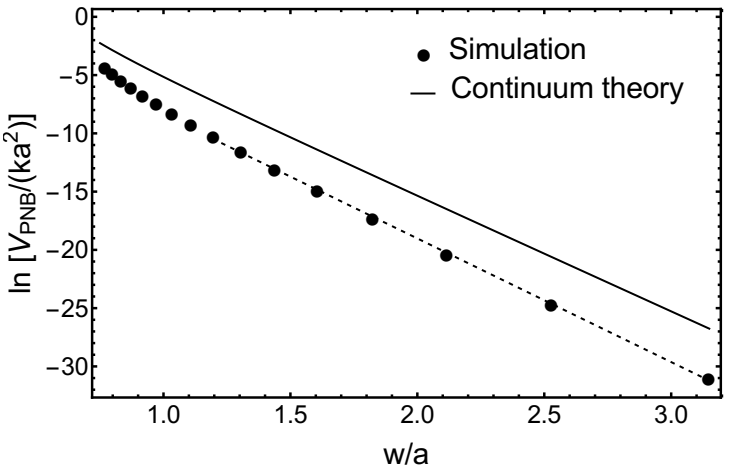

Figure 2.10. The dependence of the normalized PN barrier (V_{PNB}/ka^2) on the normalized antikink width (w/a), for both the discrete model (black circles) and the continuum theory (solid line). The slope of the dashed line (fit to simulation) is -10.6, in reasonable agreement with the predictions from the continuum theory in Eqn. (2.18), which gives a slope $-\pi^2 \approx -9.9$.

by the fact that the discreteness of the lattice is ignored in the theory when we take the continuum limit in going from Eqn. (2.8) to Eqn. (2.9). See [60] for a thorough discussion of the effect of lattice discreteness on the single-kink dynamics in a ϕ^4 model.

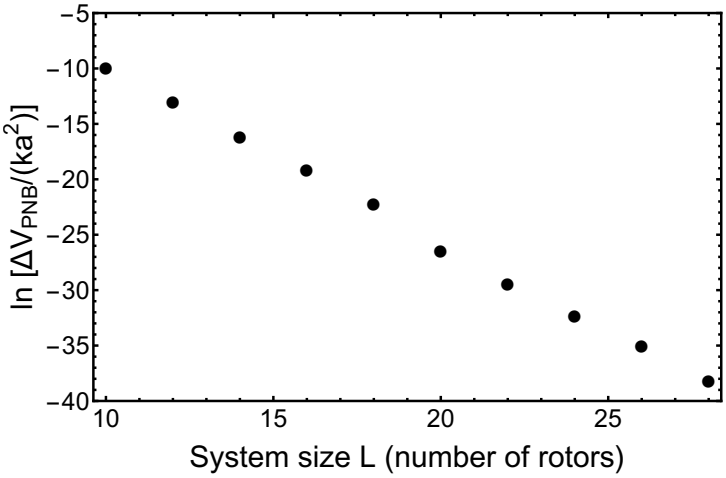

Figure 2.11. The finite-size effect on V_{PNB}. ΔV_{PNB} is defined as $V_{PNB}(L) - V_{PNB}(L = 60)$. The configuration parameters are $r/a = 0.8$ and $\overline{\theta} = 0.40$.

Further, we also investigate finite-size corrections to the PN barrier, or more precisely, the difference between V_{PNB} for a system with a small finite size and that for a system with a sufficiently larger size (60 rotors). We find that finite size effects decay quickly as an exponential function with increasing system size for a topological rotor chain with a central antikink (see Fig. 2.11). This is because an antikink configuration is a localized object. The components of its displacement, its translation mode, as well as its shape mode, decay exponentially away from its center and therefore, so does the effect of any boundaries.

To summarize, for the topological rotor chain that we study, the PN barrier for a kink vanishes and that for an antikink is finite. This, not only affects how their respective kinetic energies fluctuate over a lattice spacing, but also affects their dynamics over long distances. It is well known that ϕ^4 kinks and antikinks are non-integrable solutions [64]. Although the kinks and antikinks

are "topologically" robust objects, they still tend to dissipate energy into phonons and into shape fluctuations as they propagate. Once an antikink has lost too much kinetic energy to be able to overcome the PN barrier, it gets trapped in a PN potential minimum, as shown in Fig. 2.12. On the other hand, for the topological rotor chain that we study, the kink never gets trapped, since its PN barrier vanishes.

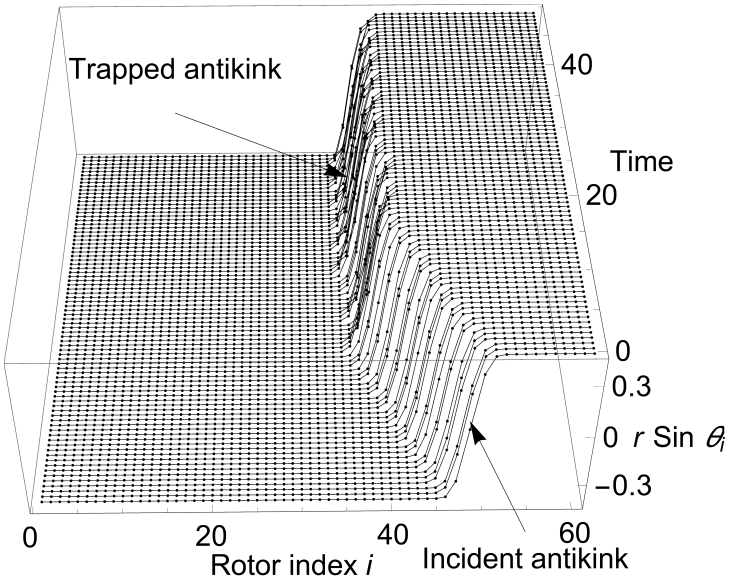

Figure 2.12. Perspective view of a moving antikink trapped in its Peierls-Nabarro barrier around Time $= 20$ near Rotor #35. The topological rotor chain has the same configuration parameters as in Fig. 2.8 and the initial antikink velocity is $v_0 = 1.1$ in non-dimensional units.

Appendix

2.A Complex notation

We use complex variables to derive the explicit relation between neighbouring rotor angles. Adopting the notation in Fig. 2.1c, we put the pivot of rotor 1 at the origin of complex plane and the pivot of rotor 2 at the coordinate (a,0). The positions of the rotor tips are

$$z_1 = ire^{-i\theta_1}, \tag{2.19}$$

$$z_2 = a - ire^{i\theta_2}. \tag{2.20}$$

We have two constraints (where a bar represents complex conjugations):

$$(z_2 - z_1)(\bar{z}_2 - \bar{z}_1) = l_0^2, \tag{2.21}$$

$$(z_2 - a)(\bar{z}_2 - a) = r^2. \tag{2.22}$$

Eliminating $\bar{z}_2$ from above two constraints, we find a quadratic equation for z_2,

$$Az_2^2 + Bz_2 + C = 0, \tag{2.23}$$

where

$$A = \frac{\bar{z}_1 - a}{a - z_1}, \tag{2.24}$$

$$B = \left(\frac{l_0^2 + a^2 - 2r^2}{a - z_1}\right) - a\left(\frac{\bar{z}_1 - z_1}{a - z_1}\right), \tag{2.25}$$

$$C = a^2 - r^2 - a\left(\frac{l_0^2 + a^2 - 2r^2}{a - z_1}\right). \tag{2.26}$$

We have two branches of the solution for z_2

$$z_2 = \frac{-B \pm \sqrt{B^2 - 4AC}}{2A}, \tag{2.27}$$

which explicitly expresses the black curve in Fig. 2.2b.

2.B Vibrational modes of prestressed mechanical structures

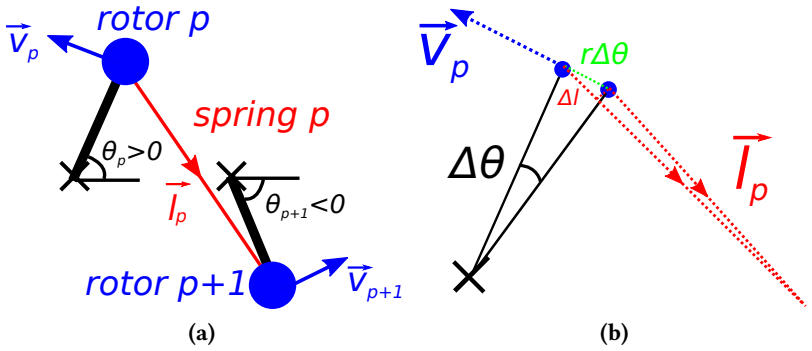

Figure 2.13. Detailed configurations around a single spring p.

We demonstrate how to use to the method of tangent stiffness matrix to calculate normal modes in prestressed mechanical structures [59].

Consider a single spring p in the configuration shown in Fig. 2.13a (note here, we are now specifying rotor angles θ with respect to the positive x-axis). From geometry, we find

$$\begin{aligned} f_p &= -\vec{v}_p \cdot \vec{l}_p \;\; \hat{t}_p \\ f_{p+1} &= \vec{v}_{p+1} \cdot \vec{l}_p \;\; \hat{t}_p. \end{aligned} \tag{2.28}$$

Here, f_p is the spring force projected along the tangent vector $\vec{v}_p$ of rotor p

$$\vec{v}_p = \begin{pmatrix} -\sin\theta_p \\ \cos\theta_p \end{pmatrix}. \tag{2.29}$$

$\vec{l}_p$ is the vector along the length of the spring p and points from rotor p to $p+1$,

$$\vec{l}_p = \begin{pmatrix} a + r\cos\theta_{p+1} - r\cos\theta_p \\ r\sin\theta_{p+1} - r\sin\theta_p \end{pmatrix}. \tag{2.30}$$

$\hat{t}_p$ is a scalar *tension coefficient* for spring p, defined as $\hat{t}_p \equiv t_p/|\vec{l}_p|$, where $t_p \equiv k_p(|\vec{l}_p| - \bar{l})$ for a harmonic spring. Here, $|\vec{l}_p|$ is the instantaneous length of spring p, $\bar{l}$ is the rest length of the spring, and k is the spring constant.

In order to find the tangent stiffness, we differentiate Eqn. (2.28) with respect to the rotor angles θ_p and θ_{p+1}

$$\frac{\partial f_p}{r\partial\theta_p} = \frac{\partial(-\vec{v}_p \cdot \vec{l}_p)}{r\partial\theta_p}\ \hat{t}_p - \vec{v}_p \cdot \vec{l}_p\ \frac{\partial \hat{t}_p}{r\partial\theta_p} \tag{2.31}$$

$$\frac{\partial f_p}{r\partial\theta_{p+1}} = \frac{\partial(-\vec{v}_p \cdot \vec{l}_p)p}{r\partial\theta_{p+1}}\ \hat{t}_p - \vec{v}_p \cdot \vec{l}_p\ \frac{\partial \hat{t}_p}{r\partial\theta_{p+1}} \tag{2.32}$$

$$\frac{\partial f_{p+1}}{r\partial\theta_p} = \frac{\partial(\vec{v}_{p+1} \cdot \vec{l}_p)}{r\partial\theta_p}\ \hat{t}_p + \vec{v}_{p+1} \cdot \vec{l}_p\ \frac{\partial \hat{t}_p}{r\partial\theta_p} \tag{2.33}$$

$$\frac{\partial f_{p+1}}{r\partial\theta_{p+1}} = \frac{\partial(\vec{v}_{p+1} \cdot \vec{l}_p)}{r\partial\theta_{p+1}}\ \hat{t}_p + \vec{v}_{p+1} \cdot \vec{l}_p\ \frac{\partial \hat{t}_p}{r\partial\theta_{p+1}}. \tag{2.34}$$

To simplify Eqn. (2.31), we express

$$\frac{\partial \hat{t}_p}{r\partial\theta_p} = \frac{\mathrm{d}\hat{t}_p}{\mathrm{d}|\vec{l}_p|}\ \frac{\partial|\vec{l}_p|}{r\partial\theta_p} \tag{2.35}$$

$$\frac{\mathrm{d}\hat{t}_p}{\mathrm{d}|\vec{l}_p|} = \frac{\mathrm{d}(t_p/|\vec{l}_p|)}{\mathrm{d}|\vec{l}_p|} = \frac{1}{|\vec{l}_p|}(g_p - \hat{t}_p) = \hat{g}_p/|\vec{l}_p|, \tag{2.36}$$

where $g_p \equiv \mathrm{d}t_p/d|\vec{l}_p|$ is defined as the axial stiffness and $\hat{g}_p \equiv g_p - \hat{t}_p$ is defined as the *modified axial stiffness*.

From Fig. 2.13b, we see that $\Delta l = r\Delta\theta\ (-\vec{v}_p \cdot \vec{l}_p)/|\vec{l}_p|$ and therefore,

$$\frac{\partial|\vec{l}_p|}{r\partial\theta_p} = \frac{(-\vec{v}_p \cdot \vec{l}_p)}{|\vec{l}_p|} \tag{2.37}$$

Substituting Eqn. (2.35 - 2.37) into Eqn. (2.31), we find

$$\frac{\partial f_p}{r\partial\theta_p} = \frac{\partial(-\vec{v}_p\cdot\vec{l}_p)}{r\partial\theta_p}\ \hat{t}_p - (\vec{v}_p\cdot\vec{l}_p)\ \frac{\hat{g}_p}{|\vec{l}_p|}\frac{(-\vec{v}_p\cdot\vec{l}_p)}{|\vec{l}_p|}. \tag{2.38}$$

Similarly, we simplify Eqns. (2.32 - 2.34)

With the above derivatives, we can now define the tangent stiffness matrix. For a single spring p, the tangent stiffness matrix, $\mathbf{K}_p$, relates small changes in rotor position to small changes in rotor forces

$$\begin{pmatrix}\delta f_p\\ \delta f_{p+1}\end{pmatrix} = \mathbf{K}_p\begin{pmatrix}r\delta\theta_p\\ r\delta\theta_{p+1}\end{pmatrix} \tag{2.39}$$

and can be expressed as

$$\mathbf{K}_p = \begin{pmatrix}n_p\\ n_{p+1}\end{pmatrix}\left[\hat{g}_p\right]\begin{pmatrix}n_p & n_{p+1}\end{pmatrix} + \mathbf{s_p}, \tag{2.40}$$

where $n_p \equiv -\vec{v}_p\cdot\vec{l}_p/|\vec{l}_p|$, $n_{p+1} \equiv -\vec{v}_{p+1}\cdot\vec{l}_p/|\vec{l}_p|$ and the *stress matrix* $\mathbf{s}_p$ is

$$\mathbf{s}_p = \begin{pmatrix} -\frac{\partial(\vec{v}_p\cdot\vec{l}_p)}{r\partial\theta_p}\ \hat{t}_p & -\frac{\partial(\vec{v}_p\cdot\vec{l}_p)}{r\partial\theta_{p+1}}\ \hat{t}_p \\ \\ \frac{\partial(\vec{v}_{p+1}\cdot\vec{l}_p)}{r\partial\theta_p}\ \hat{t}_p & \frac{\partial(\vec{v}_{p+1}\cdot\vec{l}_p)}{r\partial\theta_{p+1}}\ \hat{t}_p \end{pmatrix}. \tag{2.41}$$

To derive the total tangent stiffness $\mathbf{K}$ for the rotor chain, we first represent the tangent stiffness $\mathbf{K}_p$ in a global coordinate system as an $n\times n$ matrix, and then sum up all the $\mathbf{K}_p$ for the $n-1$ springs:

$$\mathbf{K} = \sum_{p=1}^{n-1}\mathbf{K}_p = \sum_{p=1}^{n-1}\mathbf{a}_p\left[\hat{g}_p\right]\mathbf{a}_p^T + \sum_{p=1}^{n-1}\mathbf{S}_p, \tag{2.42}$$

where

$$\mathbf{a}_p = \begin{pmatrix} 0 \\ \vdots \\ 0 \\ n_p \\ n_{p+1} \\ 0 \\ \vdots \\ 0 \end{pmatrix} \tag{2.43}$$

and

$$\mathbf{S}_p = \begin{pmatrix} \mathbf{O} & \cdots & & \mathbf{O} \\ \vdots & \mathbf{s}_{p11} & \mathbf{s}_{p12} & \vdots \\ \vdots & \mathbf{s}_{p11} & \mathbf{s}_{p12} & \vdots \\ \mathbf{O} & \cdots & & \mathbf{O} \end{pmatrix}. \tag{2.44}$$

In $\mathbf{a}_p$, the n_p and n_{p+1} terms are in the pth and $p+1$th row respectively, and all the other terms are zero. In $\mathbf{S}_p$, $\mathbf{s}_{pij}$ is the (i,j) element of the 2×2 stress matrix $\mathbf{s}_p$ for a single spring p and is located in the $(p-1+i, p-1+j)$ position of $\mathbf{S}_p$, and all the other terms in $\mathbf{S}_p$ are zero. Here $\mathbf{S}_p$ has a simpler form than that of Ref. [59] because we exploit the fact that only nearest neighbours are coupled in the topological chain.

2.C Simulation methods

We carry out the molecular dynamics simulations in Mathematica. The ODEs are solved by the function NDSolve, which uses a multi-step method (LSODA) by default.

In the simulations, we set the lattice spacing $a = 1$, the rotor mass $M = 1$, and an arbitrary time unit $t = 1$. The spring constant k is measured in units of M/t^2. The linear velocity of a rotor is measured in units of a/t. The initial velocity v_0 of a (anti)kink is defined as the velocity amplitude of the unit translation mode $\mathbf{e}^t$ and e_i^t is the mode component on the i-th rotor. Thus the initial kinetic energy is $\Sigma_i \frac{1}{2} m (v_0 e_i^t)^2 = \frac{1}{2} m v_0^2$.

2.D Peierls-Nabarro potential barrier via continuum theory

We derive the PN potential by discretizing the potential energy density in the continuum theory, i.e. taking the quasi-continuum limit. The PN potential is, by definition, the potential that the kink faces as it propagates along the adiabatic trajectory (ad. tr.) :

$$V_{PN}(X) = V(..., u_{n-1}, u_n, u_{n+1}, ...)|_{X \in ad.tr.}. \tag{2.45}$$

Here, X is the position of the (anti)kink center, u_n is the continuum field at lattice site n, V is a discretization of the potential energy density $V(\theta)$ in Eqn. (2.9) and is obtained by summing the potential $f(n, X)$ of each lattice site:

$$V(..., u_{n-1}, u_n, u_{n+1}, ...) = \sum f(n, X), \tag{2.46}$$

where

$$f(n, X) = \frac{2k}{\bar{l}^2}\left(\frac{a^2}{2}\frac{\mathrm{d}u_n}{\mathrm{d}(na)} + \overline{u}^2 - u_n^2\right)^2. \tag{2.47}$$

$f(n, X)$ is the approximate potential at a single site n when the (anti)kink center is at X. Here, we discretize the continuum potential energy density rather than directly use the exact form of the lattice potential in Eqn. (2.8), so that we can readily substitute u_n, the continuum field at site n, into $f(n, X)$ which results in an integrable solution. We choose the static solution ($v = 0$) of Eqn. (2.13) as the adiabatic trajectory:

$$u_n(X) = \pm\overline{u}\tanh\left(\frac{na - X}{w}\right), \tag{2.48}$$

where the "$+$" is for the antikink, "$-$" is for the kink, and the width of the (anti)kink $w = \frac{a^2}{2r\sin\overline{\theta}}$ [18]. Substituting Eqn. (2.48) into Eqn. (2.47), we find

$$\begin{aligned} f(n, X) &= 0 && \text{for the kink,} \\ f(n, X) &= \frac{8k\overline{u}^4}{\bar{l}^2}\operatorname{sech}^4\left(\frac{na - X}{w}\right) && \text{for the antikink.} \end{aligned} \tag{2.49}$$

Thus $V_{PN}(X) = 0$ for the kink, in accordance with the fact that the kink configuration does not stretch springs and hence costs zero potential energy. For the antikink, we use the Poisson summation formula to express:

$$\begin{aligned} V_{PN}(X) &= \sum_{n=-\infty}^{+\infty} f(n, X) = \sum_{k=-\infty}^{+\infty} \hat{f}(k, X) \\ &= \sum_{k=-\infty}^{+\infty} \int_{-\infty}^{+\infty} \mathrm{d}n f(n, X) e^{-2\pi i k n}. \end{aligned} \tag{2.50}$$

To leading order, we only consider the first harmonic terms $k = 1$ and $k = -1$ ($k = 0$ recovers the continuum approximation). For $k = 1$, we find

$$\begin{aligned} &\int_{-\infty}^{+\infty} \mathrm{d}n f(n, X) e^{-2\pi i n} \\ &= e^{-2\pi i (X/a)} \int_{-\infty}^{+\infty} \mathrm{d}n' \frac{8k\overline{u}^4}{\bar{l}^2} \operatorname{sech}^4\left(\frac{n'a}{w}\right) e^{-2\pi i n'}. \end{aligned} \tag{2.51}$$

The complex exponential suggests a sinusoidally varying potential along the coordinate X of the adiabatic trajectory, with a period that is equal to the lattice spacing a. We define the *PN barrier* (V_{PNB}) as the height of this sinusoidal potential. The last integral in Eqn. (2.51) can be completed using residues to yield

$$\begin{aligned} V_{PNB} &= \frac{4\pi^2\Big(\pi^2 + (a/w)^2\Big)}{3\Big(1 + 4(r/a)^2 - (a/w)^2\Big)\sinh(\pi^2 w/a)} \\ &\propto e^{-\pi^2 w/a} \qquad \text{for large } w/a. \end{aligned} \tag{2.52}$$